

# Effects of periodic forcing on a Paleoclimate delay model\*

Courtney Quinn<sup>†</sup>, Jan Sieber<sup>†</sup>, and Anna von der Heydt<sup>‡</sup>

**Abstract.** We present a study of a delay differential equation (DDE) model for the Mid-Pleistocene Transition. We investigate the behavior of the model when subjected to periodic forcing. The unforced model has a bistable region consisting of a stable equilibrium along with a large amplitude stable periodic orbit. We are interested in how forcing affects solutions in this region. The results here are compared to what is found when the model is forced with the quasiperiodic insolation. The quasiperiodic forcing displays a threshold behavior when the forcing amplitude is increased - moving the model from a non-transitioning regime to a transitioning regime. Similar threshold behavior is found when the periodic forcing amplitude is increased. A bifurcation analysis shows that the threshold is not due to a bifurcation but instead to a shifting basin of attraction.

**Key words.** delay, paleoclimate, bifurcation, Mid-Pleistocene Transition, equation-free methods, dimension reduction

**AMS subject classifications.** 37M20, 86A04, 37C55, 37B55, 34K28

**1. Introduction.** Low-dimensional conceptual models are often used in climate modelling to understand basic interactions between specific climate variables [8]. These are particularly useful when studying long time-scale dynamics and computing power precludes resolving all of the many temporal and spatial scales [18]. For this reason, conceptual models are essential in studying past climates of the earth and their long-term variability.

The Pleistocene, which lasted from approximately 2.6 Myr to 11.7 kyr before present, is a period in climate history that particularly benefits from this type of modelling. The essential variability can be captured through dynamical systems with only a few coupled variables (see review [6] for an extensive collection of examples). During this time, the earth experienced many oscillations between periods of colder temperatures and increased global ice cover (*glacials*) and periods of warmer temperatures with less global ice cover (*interglacials*) [17]. The dominant periodicity of the oscillations also changed from approximately 41 kyr in the beginning of the Pleistocene to roughly 100 kyr towards the end of the Pleistocene, together with an increase in amplitude and degree of asymmetry in the oscillations [14, 22]. This shift in dynamics is known as the Mid-Pleistocene Transition (MPT), and the exact timing of it is believed to be sometime between 1200 and 700 kyr BP [22, 28, 6, 8, 11]. The oscillations and the MPT can be observed through proxy records as shown in Figure 1.

---

\*Submitted to the editors 26 July 2018.

**Funding:** C.Q. and J.S have received funding from the European Union's Horizon 2020 research and innovation programme under the Marie Skłodowska-Curie grant agreement No 643073. J.S. gratefully acknowledges the financial support of the EPSRC via grants EP/N023544/1 and EP/N014391/1. AvdH gratefully acknowledges financial support from the EPSRC funded Past Earth Network (grant number EP/M008363/1) and ReCoVER (grant number EP/M008495/1) for an extended research visit to the University of Exeter in summer 2017.

<sup>†</sup>College of Engineering, Mathematics, and Physical Sciences, University of Exeter, Exeter EX4 4QE, United Kingdom (c.quinn2@exeter.ac.uk, J.Sieber@exeter.ac.uk).

<sup>‡</sup>Institute for Marine and Atmospheric Research, Department of Physics & Center for Complex Systems Studies, Utrecht University, Princetonplein 5, 3584 CC Utrecht, The Netherlands (A.S.vonderHeydt@uu.nl).

In a recent study [29] we revisited a model of the Pleistocene introduced by Saltzman and Maasch [30]. This model was used to replicate the main dynamics of the ice ages, which involved perturbations in glacial ice mass, atmospheric  $\text{CO}_2$ , and global ocean circulation. In the original study, the authors of [30] showed this particular model was able to reproduce the MPT through a slow parameter shift. In our study [29] we reduced this model to a scalar delay differential equation (DDE) for global ice mass. Through analytical and numerical investigations we showed that the models were qualitatively equivalent. Our main focus of the study was on the bistable region found in both the original ODE model and the DDE model, a region which was not explored in the original analyses [30, 23]. We observed the behavior within this region when the model was subjected to external forcing, namely solar radiation, and were able to reproduce a MPT-like transition without any change in parameters.

Very early studies have shown a relationship between solar radiation and the glacial cycles [26, 4, 32]. The solar radiation, otherwise known as astronomical insolation, is a quasiperiodic forcing with dominant frequencies around 0.0243, 0.0434, and 0.0526  $\text{kyr}^{-1}$ , corresponding to periodicities of 41, 23, and 19  $\text{kyr}$  respectively (see Figure 1) [2, 15]. The most prominent signal in the forcing is at 41  $\text{kyr}$ , and this has been argued to be the driving force of the climate fluctuations in the beginning of the Pleistocene [26], while it remains still unclear where the longer-term and large-amplitude fluctuations of the late Pleistocene derive from and why a transition from the 41  $\text{kyr}$  to the 100  $\text{kyr}$  dominant periodicity occurred [27]. It is natural then to consider the effects of the 41  $\text{kyr}$  signal alone on our model. In this paper we perform a systematic study of how the model responds to periodic forcing with a period of 41  $\text{kyr}$ .

The paper is organized as follows. We summarize the numerical observations and the bifurcation analysis of the unforced system from our recent study [29] in section 2. Section 3 studies the effects of periodic forcing, showing that one type of transition observed in [29] can be attributed to a shift in basin boundaries in the context of periodic forcing. We are able to track the precise basin boundary by applying algorithms developed for stable manifolds of two-dimensional maps to the forced DDE. Section 4 compares our results to other hypotheses, also suggesting how the theory for quasiperiodically forced systems could be applied to extend our results.

**2. Background.** Our delay equation model of global ice mass perturbations as described in [29] is as follows:

$$(1) \quad \dot{X}(t) = -pX(t - \tau) + rX(t) - sX(t - \tau)^2 - X(t - \tau)^2X(t).$$

Here,  $X$  represents the ice mass anomaly from a background state where  $X(t)$  and  $X(t - \tau)$  are taken at present and  $\tau$  years in the past, respectively. The delay  $\tau$  is the timescale of the feedback processes associated with ice accumulation and decay, and carbon storage and transport in the deep ocean. This is the parameter we are most interested in analysing. The other parameters  $p$ ,  $r$ , and  $s$  will be kept constant at  $p = 0.95$ ,  $r = 0.8$ , and  $s = 0.8$  in accordance with [30] for all numerical studies.

This is not the first time a delay model has been suggested for the dynamics of the Pleistocene. Bhattacharya *et al.* [3] explored an energy balance model which incorporates a delay related to feedback effects from the reflectivity of the earth's surface. Additionally, Ghil *et al.* [13] proposed a Boolean delay model for global temperature, northern hemisphere

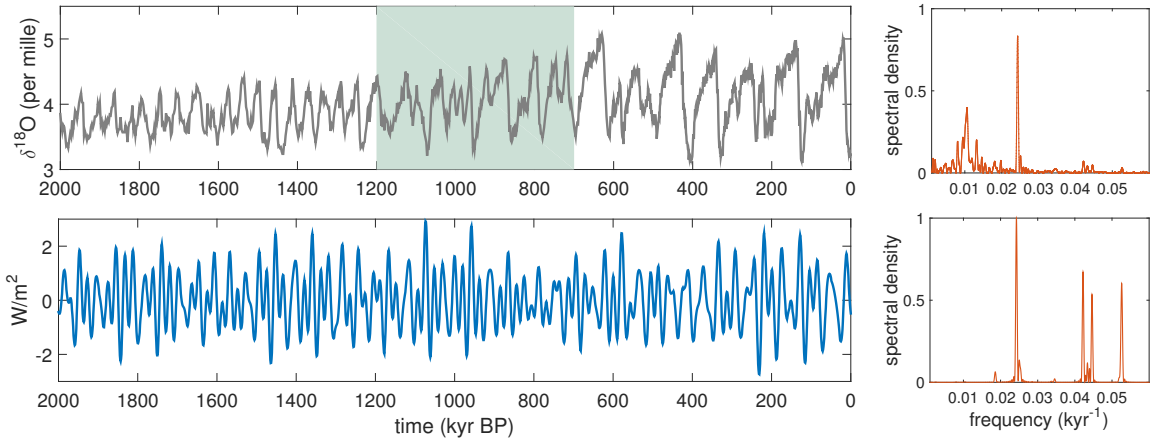


Figure 1: (Top) Proxy record of global ice cover for the last 2 Myr [21] and its spectrum. (Bottom) Normalized integrated July insolation  $F_I(t)$  at 65°N, adapted from [16], and its spectrum.

ice volume, and deep-ocean circulation, with delays corresponding to ice sheet expansion, ice accumulation, and overturning time of the deep ocean. The three delay effects discussed in [13] are captured within our delayed feedback model.

**2.1. Internal Dynamics.** We conducted a bifurcation analysis of the model for realistic values of the delay,  $\tau \in (1, 2)$ . There were five distinct regions with respect to global stability (see Figure 2). They are as follows:

- $[r_{ee}]$  two stable equilibria,
- $[r_{es}]$  one stable equilibrium and one stable small-amplitude periodic orbit,
- $[r_e]$  one stable equilibrium,
- $[r_{el}]$  one stable equilibrium and one stable large-amplitude periodic orbit, and
- $[r_l]$  one stable large-amplitude periodic orbit.

The bistable region,  $r_{el}$ , for  $\tau \in [1.295, 1.625]$  with a stable equilibrium and a large amplitude stable periodic orbit was previously not explored. Within this region, if the model is subjected to external forcing, transitions are possible between the two stable states without any change in parameters.

We also make a note about the dimensionality of the system. Although DDEs are infinite-dimensional, the phase portrait in Figure 2 gives initial evidence that the dynamics are confined to a two-dimensional slow manifold. Engler *et al.* [11] derived a two-dimensional slow manifold for the original model [30] through considering the deep ocean timescale as instantaneous. The dimensionality will be investigated in more detail in Section 3.2.

**2.2. Astronomical Forcing.** In [29] we were interested in the model's response in the bistable region when subjected to astronomical forcing. We included this effect as additive forcing (with negative amplitude as insolation reduces ice mass),

$$(2) \quad \dot{X}(t) = -pX(t - \tau) + rX(t) - sX(t - \tau)^2 - X(t - \tau)^2X(t) - uF_I(t).$$

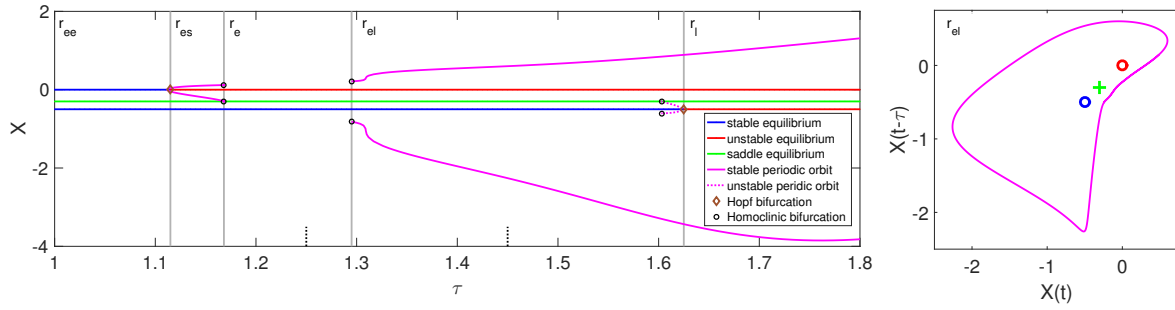


Figure 2: (Left) Bifurcation diagram of the DDE model for delay parameter  $\tau$ . The dotted black lines indicate values of  $\tau$  used in forcing studies:  $\tau_{\text{ref}} = 1.25$  and  $\tau_{\text{bist}} = 1.45$ . Figure adapted from [29]. (Right) Phase portrait of the bistable region  $r_{\text{el}}$ ,  $\tau_{\text{bist}} = 1.45$ . The circles are the stable (blue) and unstable (red) equilibria, the green cross is the saddle equilibrium, and the pink curve shows the periodic orbit. Other parameters:  $p = 0.95$ ,  $r = s = 0.8$ .

The  $F_I(t)$  is the forcing signal, shown in Figure 1, which is a time series of integrated summer insolation at 65°N computed by [16] based on the model in [15]. Details, how the forcing curve in Figure 1 was obtained from publicly available data, are given in [29]. This is a quasiperiodic forcing, with dominant frequencies corresponding to periods of around 41, 23, and 19 kyr (as shown in Figure 1). The parameter  $u$  represents the forcing amplitude of which the exact physical value is uncertain.

Figure 3a shows the response of the bistable region for many values of the forcing amplitude  $u$ . For values of  $\tau$  in the bistable region, there are two possible responses for small  $u$ : a *small-amplitude* and a *large-amplitude* response. Each response is a perturbation of an attractor of the unforced system, namely the equilibrium and the large-amplitude periodic orbit, which persist for small  $u$ . These responses can be seen by comparing the red and blue time profiles in Figure 3b. The red time profile is computed outside of the bistable region, where only the small-amplitude response exists. The blue time profile shows a small-amplitude response (with an excursion) up until about 800 kyr BP, when it then transitions to the large amplitude response. This is one example of a solution that displays a mid-Pleistocene transition. The supplementary material includes a video of the blue and red trajectories as they change with increasing  $u$ , where more examples of MPT-like transitions can be seen.

Figure 3a illustrates the transitions that can be seen over a large range of forcing strengths  $u$ . Two prominent transitions are visible: one with respect to time and the other with respect to forcing strength. The former of these two was briefly discussed in [29] along with its relation to climate records. This is the transition that appears to occur consistently between 700 and 800 kyr BP which agrees with the timing of the MPT. The fact that the system favors this time period to transition is beyond the scope of this paper. In this study we will focus on the latter of the two transitions, the one with respect to forcing strength  $u$ , and attempt to explain it through analysing the model under periodic forcing. This transition relates to the first in the sense that we intend to explain the range of forcing amplitudes that allows a temporal transition similar to the MPT (possibly timed by a distinct property of the astronomical

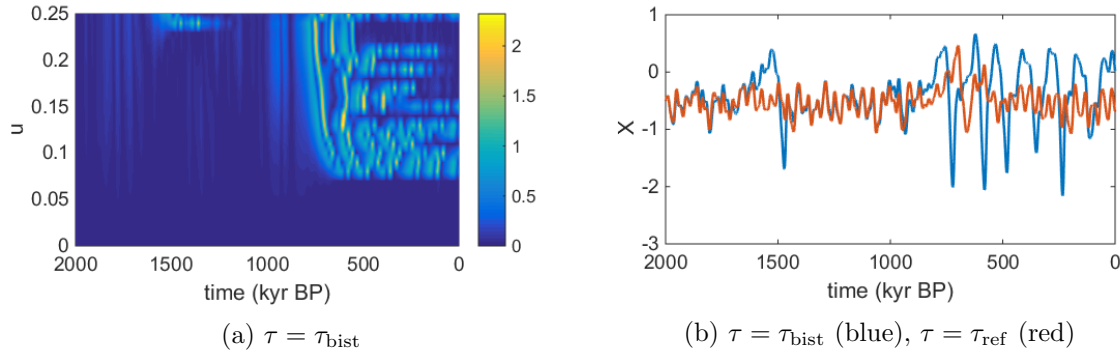


Figure 3: *Small-amplitude* and *large-amplitude* responses observed in bistable region when subjected to astronomical forcing. (a) Distance of trajectories in bistable region from reference trajectory at  $\tau_{\text{ref}} = 1.25$ , for different forcing strengths  $u$ . Averages taken over window length of size  $\tau_{\text{bist}}$ . (b) Trajectory in bistable region (blue) for  $\tau_{\text{bist}} = 1.45$  compared to a reference trajectory at  $\tau_{\text{ref}} = 1.25$  (red) for  $u = 0.25$ . Initial condition  $X(t) = -0.5$  for  $t \leq 0$ . Other parameters:  $p = 0.95$ ,  $r = s = 0.8$ . Figures adapted from [29].

forcing around the transition).

**3. Periodic Forcing.** We are interested in the behavior of this model when a sinusoidal forcing with period 41 kyr is included. This corresponds to the most prominent frequency found in orbital forcing - the obliquity variations, *i.e.* the changes in the angle between the rotational and orbital axes. Thus, we choose

$$(3) \quad F_P(t) = \sin(2\pi t/T).$$

The forcing period is  $T = 4.1$ , corresponding to 41 kyr.

This forcing is included in the same way as the astronomical forcing  $F_I$ ,

$$(4) \quad \dot{X}(t) = -pX(t - \tau) + rX(t) - sX(t - \tau)^2 - X(t - \tau)^2X(t) - uF_P(t).$$

DDE (4) is a dynamical system with the phase space  $U = C([-\tau, 0]; \mathbb{R})$ , where  $C([-\tau, 0]; \mathbb{R})$  is the space of continuous functions on the interval  $[-\tau, 0]$  with the maximum norm  $\|X\|_0 = \max\{|X(t)| : t \in [-\tau, 0]\}$ . At any given time  $t \geq 0$ , the state is  $X_t : [-\tau, 0] \ni s \mapsto X(t+s) \in \mathbb{R}$ . For sufficiently small values of  $u$  and  $\tau \in r_{\text{el}}$ , there exist

- a stable small amplitude periodic orbit (with period  $T$ ), which is a perturbation of the stable equilibrium at  $u = 0$ , and
- a stable quasiperiodic large amplitude solution, which is a perturbation from the large amplitude periodic orbit at  $u = 0$ .

These two attractors will persist for a range of  $u$  and we will refer to them as the *small-amplitude response* and the *large-amplitude response*, as we did in the case of astronomical forcing. Both types of stable long-time regimes are shown in Figure 4a including a transient. We observed in simulations that the large-amplitude response changes from quasiperiodic to

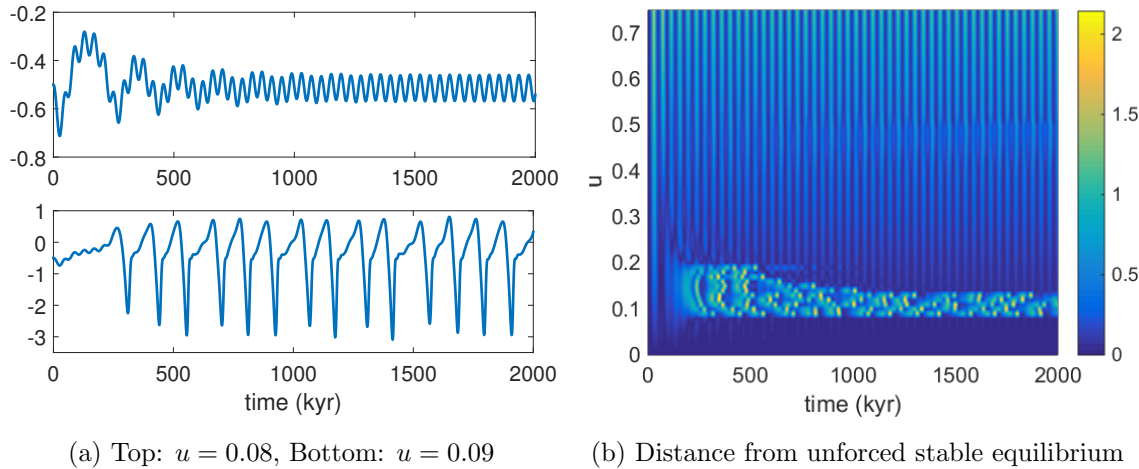


Figure 4: (a) Example trajectories of (4) for two qualitatively different long-time regimes. Top: small-amplitude response (a small-amplitude periodic orbit), bottom: large-amplitude response (longer time series suggest that it is chaotic). (b) Distance of solution  $X$  from  $X : s \mapsto -0.5$  (a stable equilibrium of the unforced system) for varying forcing amplitudes  $u$ . Other parameters:  $\tau = 1.55$ ,  $T = 4.1$ ,  $p = 0.95$ ,  $r = s = 0.8$ ,  $\phi = 0$ ; initial condition  $X(t) = -0.5$  for  $t \leq 0$ .

chaotic as  $u$  increases. Large-amplitude chaotic responses have been observed previously in conceptual ice age models subject to periodic forcing in the literature. Ashwin *et al.* [1] find significant regions of chaotic responses for the van der Pol-Duffing oscillator, the Saltzman and Maasch 1991 model [31], and the Paillard and Parrenin 2004 model [28]. The chaos exists both for simple periodic forcing defined by (3) and more complex quasiperiodic forcings. In contrast to our scenario, in [1] all of the models were considered in parameter regions where the unforced dynamics has a single large-amplitude stable periodic orbit. Our simulations suggest that large-amplitude chaotic solutions are also present in a periodically forced bistable regime.

The heat map in Figure 4b shows the model response over a larger range of forcing amplitudes  $u$ . For Figure 4b we keep the delay constant at  $\tau = 1.55$  and increase  $u$  from 0 to 0.75. All trajectories start from the constant initial history  $X_0 : [-\tau, 0] \ni s \mapsto -0.5 \in \mathbb{R}$  corresponding to the stable equilibrium of the unforced system. We then compute the distance of  $X_t : [-\tau, 0] \ni s \mapsto X(t+s) \in \mathbb{R}$  to  $X_0$ , using the mean absolute error (MAE),  $\text{MAE}(X_t, X_0) = \frac{1}{\tau} \int_{-\tau}^0 |X_t(s) - X_0(s)| ds$ . Bright colors in Figure 4b indicate large distances, corresponding to large amplitude responses. We notice an obvious shift in behavior between  $u = 0.08$  and  $u = 0.09$  where the model goes from exhibiting the small-amplitude periodic orbit to following the large-amplitude solution. This lower threshold is similar to the observations when applying non-periodic insolation forcing (compare to Figure 3a).

**3.1. Bifurcation analysis.** In order to examine the cause of the shift in behavior observed in Figure 4b, we start a numerical bifurcation analysis of DDE (4). The forcing period is kept

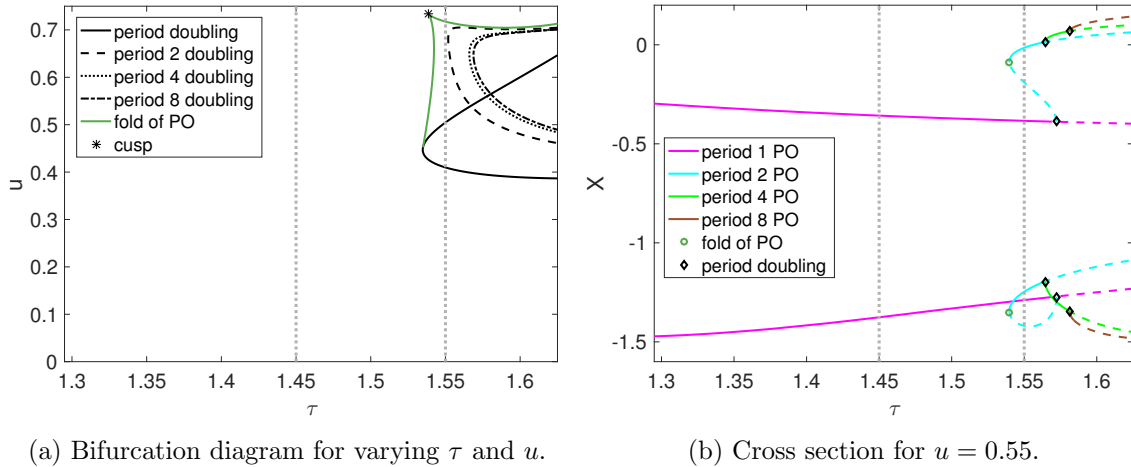


Figure 5: Bifurcations of small-amplitude periodic orbit. Dotted vertical lines indicate values of  $\tau$  used in subsections 3.2 to 3.4; other parameters:  $T = 4.1$ ,  $\tau = 1.55$ ,  $p = 0.95$ ,  $r = s = 0.8$ .

constant at  $T = 4.1$  (corresponding to 41 kyr). We consider forcing amplitudes  $u \in [0, 0.75]$  and delays  $\tau$  in the bistable region  $\tau \in r_{\text{el}} \approx [1.295, 1.625]$  of the unforced system ( $u = 0$ ).

Figure 5a shows the bifurcations of the small-amplitude periodic orbit. Bifurcations only occur for  $\tau > 1.53$  and  $u > 0.38$ . For a range of  $u > 0.4$  there exists a cascade of period doubling bifurcations for increasing  $\tau$ , evidence of which is also visible in Figure 4b. Figure 5b shows a cross section of the two-parameter bifurcation diagram Figure 5a along the horizontal line  $u = 0.55$  displaying the maximum and minimum of the periodic orbits on the  $y$ -axis. We observe that the small-amplitude motion does *not* experience any bifurcation for  $u < 0.3$ . Moreover, because the bifurcations are restricted to large values of  $\tau$ , they cannot be used to explain the transition in time observed in Figure 3a, which is present for all  $\tau$  throughout the bistable region; see [29]. Therefore periodic forcing, even with a time-dependent modulated amplitude, is not sufficient to induce the MPT-like transition.

The large amplitude solution also goes through some bifurcations. We do not show a detailed bifurcation analysis, but evidence of the collapse of the large amplitude solution can be seen in Figure 4b. These large responses are stable in a range of forcing amplitudes  $u \in [0.09, 0.15]$  in Figure 4b. For  $u \in [0.15, 0.2]$  the trajectories make transient large-amplitude excursions before converging to a small-amplitude periodic orbit, which suggests a collapse of the (then chaotic) large-amplitude attractor.

As Figure 5a establishes, the observed transition in Figure 4b from small- to large-amplitude oscillations at  $u = 0.09$  must have been caused by some phenomenon other than a bifurcation. Since the unforced system is bistable for  $\tau \in r_{\text{el}}$ , we expect this bistability to persist for small forcing amplitudes  $u$ . Thus, the initial condition may cross from the basin of attraction of the small-amplitude periodic orbit to the basin of attraction of the large-amplitude response. Both example trajectories in Figure 4a started from the same initial condition but were computed with slightly different forcing amplitude ( $u = 0.08$  and

$u = 0.09$ ). Figure 4b suggests that the constant initial condition  $X_0 : s \mapsto -0.5$  leaves the basin of attraction of the small-amplitude periodic orbit at the lower threshold  $u \approx 0.09$ .

**3.2. Dynamics on a two-dimensional slow manifold.** Since DDEs are infinite-dimensional, it is not feasible to determine the basin of attraction in all dimensions. However, previous studies have proven results of Poincaré-Bendixson type (there exists a plane in  $\mathbb{R}^2$  such that trajectories cannot cross each other) for scalar DDEs with monotone feedback [25, 24]. These are DDEs of the form

$$(5) \quad \dot{x}(t) = f(x(t), x(t - \tau)), \quad \text{where } f(0, 0) = 0 \text{ and } \delta y f(0, y) > 0 \text{ for all } y \neq 0, \delta \in \{-1, 1\},$$

( $\delta = 1$  corresponds to positive delayed feedback,  $\delta = -1$  corresponds to negative delayed feedback). The right-hand side  $f(X(t), X(t - \tau))$  in (1) does not satisfy the feedback conditions in (5) since, for our right-hand side  $f$ ,  $f(0, y) = -py - sy^2$  changes sign also at  $y = -p/s = -1.1875$ , which is reached in the unforced large-amplitude periodic orbit (see Figure 2). However, the phase portrait in Figure 2 suggests that the unforced DDE (4) (with  $u = 0$ ) has an attracting two-dimensional slow manifold. We expect this manifold to persist for small forcing amplitudes  $u$ . Within this persistent slow manifold the time- $T$  map of the forced DDE (4) is a locally invertible two-dimensional map. For two-dimensional maps the basin of attraction for a periodic orbit is often bounded by the stable manifold of a saddle periodic orbit. We can investigate the basin of attraction directly by using an implicit computational dimension reduction introduced by Kevrekidis *et al* as *equation-free methods* (see reviews [19, 20]). In their notation one needs to define the following operators. Recall that  $U = C([-\tau, 0]; \mathbb{R})$  is the phase space of the DDE (4).

$$(6) \quad \text{lifting} \quad L : \mathbb{R}^2 \ni (x_1, x_2) \mapsto (y_0, \tilde{y}) \in \mathbb{R} \times \mathbb{L}^\infty([-\tau, 0]; \mathbb{R}),$$

where  $y_0 = x_1$  and  $\tilde{y}(t) = x_2$  for  $t \in [-\tau, 0]$ ,

$$(7) \quad \text{evolution map} \quad M : [0, \infty) \times [0, \infty) \times \text{rg } L \ni (t_0 + t, t_0, (y_0, \tilde{y})) = X_{t_0} \mapsto X_{t+t_0} \in \text{rg } L,$$

$$(8) \quad \text{restriction} \quad R : U \ni X \mapsto (X(0), X(-\tau))^T \in \mathbb{R}^2.$$

The space  $\mathbb{R} \times \mathbb{L}^\infty([-\tau, 0]; \mathbb{R})$  (called  $U^{\odot,*}$  in the terminology of [7]) is a natural extension of the phase space  $U = C([-\tau, 0]; \mathbb{R})$  of the DDE (4). The trajectories of the DDE (4) starting from initial values in  $U^{\odot,*}$  admit discontinuous essentially bounded initial history segments  $\tilde{y} : [-\tau, 0] \mapsto \mathbb{R}$  and have  $y_0$  as the right-side limit for  $t \searrow 0$ . For an element  $(y_0, \tilde{y})$  of  $U^{\odot,*}$ ,  $y_0$  is usually called the *head point*, while  $\tilde{y}$  is the *history segment*. The notation  $\mathbb{L}^\infty([-\tau, 0]; \mathbb{R})$  refers to the space of essentially bounded functions on  $[-\tau, 0]$  with essential maximum norm  $\|\tilde{y}\|_0 = \inf \{m \geq 0 : \text{Leb}\{t \in [-\tau, 0] : |\tilde{y}(t)| \geq m\} = 0\}$  (Leb  $A$  is the Lebesgue measure of a set  $A \subset \mathbb{R}$ ). As explained in the textbook [7] trajectories starting from an element in the larger space  $U^{\odot,*}$  return to the smaller phase space  $U$  after time  $\tau$  and the dependence  $U^{\odot,*} \ni X_0 \mapsto X_t \in U$  of the solution on its initial condition is as regular as the right-hand side of the DDE (4). Thus,

$$U^{\odot,*} \ni X \mapsto M(t, t_0; X) \in U$$

is smooth for all  $t \geq \tau$  and  $t_0 \in \mathbb{R}$ .

In our computations we approximate elements  $(y_0, \tilde{y}) \in U^{\odot,*}$  by vectors  $Y \in \mathbb{R}^N$ , where  $Y_k$  is an approximation of  $\tilde{y}(-\tau(N-k)/(N-1))$  for  $1 \leq k < N$  and the head point is  $Y_N = y_0$ . We use the discretized map  $M$  based on the Euler-Heun approximation with  $h = 0.01$ , where a single step has the form

$$\begin{aligned} M(h, t, \cdot) : \mathbb{R}^N &\ni Y \mapsto (Y_2, \dots, Y_N, Y_N + h(f_0 + f_E)/2)^T \in \mathbb{R}^N, & \text{where} \\ f_0 &= f(t, Y_N, Y_1, u), \quad Y_N^0 = Y_N + h f_0, \quad f_E = f(t + h, Y_N^0, Y_2, u), & \text{and} \\ f(t, x_1, x_2, u) &= -px_2 + rx_1 - sx_2^2 - x_2^2 x_1 - u F_P(t) \end{aligned}$$

is the right-hand side of the DDE (4). For larger time spans we apply the composition rule  $M(t + s, r, \cdot) = M(t, s + r, \cdot) \circ M(s, r, \cdot)$  for  $s, t \geq 0$ , such that the discretization using  $N-1 = s/h$  steps converges to the continuous map  $M(t + s, s, \cdot)$  uniformly for bounded  $t \geq \tau$  and bounded initial values in  $U^{\odot,*}$ . We restrict ourselves to stroboscopic maps  $M(t + s, s, \cdot)$ , where  $t$  is a multiple of the period:  $t = kT$  with  $k \in \mathbb{Z}$  and  $T = 4.1$ , such that we may write

$$M^k Y = M(kT, 0, Y)$$

for integers  $k \geq 0$ . The map  $M^k : \text{rg } L \rightarrow \text{dom } R$  ( $\text{rg } L$  is the range of  $L$ ,  $\text{dom } R$  is the domain of definition of  $R$ ) is autonomous and smooth, since  $M((k+j)T, jT, \cdot) = M(kT, 0, \cdot)$  for all integers  $k \geq 0$  and  $j$ , and periodic forcing with period  $T$ . With this notation,  $M^{k+j}$  equals  $M^k M^j$ . Compatible with the discretization of  $M$ , the discretizations of lifting and restriction are

$$\begin{aligned} L : \mathbb{R}^2 &\ni (x_1, x_2)^T \mapsto (x_2, \dots, x_2, x_1)^T \in \mathbb{R}^N, \\ R : \mathbb{R}^N &\ni Y \mapsto (Y_N, Y_1)^T \in \mathbb{R}^2. \end{aligned}$$

Figure 6a shows that the linearization of the map  $M^1$  has a spectral gap after the first two eigenvalues such that  $\partial M^1$  is a small perturbation of a rank 2 matrix for all  $y$  in a neighborhood of  $L([-0.75, 0.15] \times [-0.75, 0.15])$ . This is numerical evidence for the suspected time scale separation leading to a two-dimensional slow manifold. We do not need to construct the slow manifold explicitly, but rather may construct an approximate two-dimensional map  $\mathcal{M}_\ell$  from the slow manifold back to itself implicitly, using the coordinates in  $\text{dom } L$ :

$$(9) \quad \mathcal{M}_\ell : \text{dom } L \ni x \mapsto y \in \text{dom } L, \quad \text{where } y \text{ is the solution of } RM^{\ell+1} L x = RM^\ell L y.$$

The integer  $\ell$  is the *healing time* in the notation of [19, 20]. The map  $\mathcal{M}_\ell$  approximates the true stroboscopic map generated by the DDE (4) on the slow manifold [33]. The approximation improves for increasing healing time  $\ell$  if lifting  $L$  and restriction  $R$  satisfy some genericity conditions (implying that the map  $R$  is a diffeomorphism between the slow manifold and  $\mathbb{R}^2$ , and that  $RM^\ell L : \mathbb{R}^2 \rightarrow \mathbb{R}^2$  is a diffeomorphism). The convergence result in [33] does not require a large separation of time scale, only a sufficiently large healing time. In our case  $\ell = 1$  (a healing time of one period  $T = 4.1$ ) is sufficient: the results only change by less than  $10^{-2}$  when increasing  $\ell$  to 2 (a large  $\ell$  increases the condition number of  $\partial[RM^\ell L]$ ).

Figure 6a justifies using a planar rectangle in  $\text{dom } L$  to visualize the basins of attraction in the slow manifold. Furthermore, since we can evaluate the stroboscopic map on the

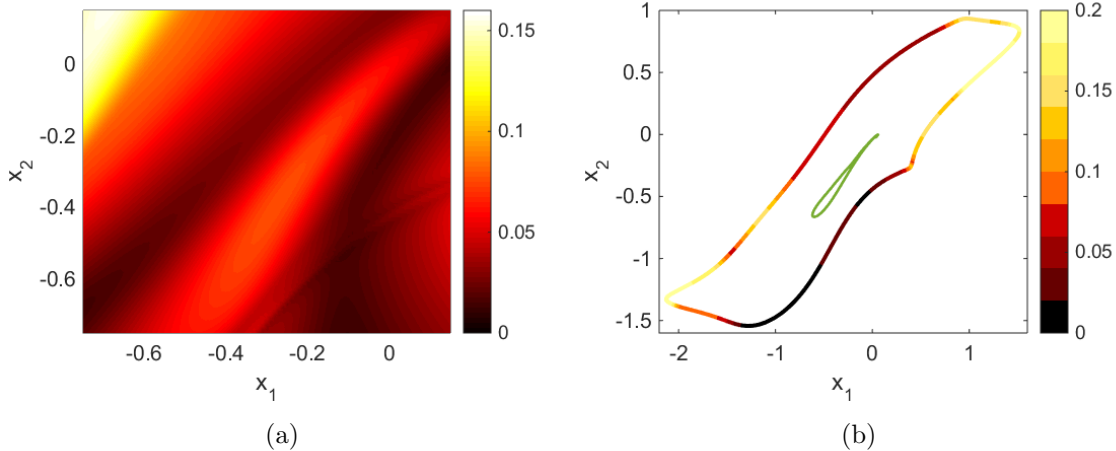


Figure 6: Spectral gap of linearization of  $M^1$  (a) on the domain  $L$  ( $[-0.75, 0.15] \times [-0.75, 0.15]$ ) and (b) on the boundary for which the Jacobian of  $RM^1L$  becomes singular. Color indicates the ratio between the third and second largest singular values of  $\partial M^1$ . The green boundary in figure (b) depicts the basin discussed in subsections 3.3 and 3.4. Parameters:  $u = 0.09$ ,  $T = 4.1$ ,  $\tau = 1.55$ ,  $p = 0.95$ ,  $r = s = 0.8$ ,  $\phi = 0$ .

two-dimensional slow manifold by using  $\mathcal{M}_\ell$ , we can employ algorithms designed for the computation of stable manifolds of fixed points in planar maps. In particular, we continue all three fixed points present for zero forcing ( $u = 0$ ; see Figure 2) in the parameter  $u$ , using the defining equation

$$RM^\ell Lx_{\text{fix}} = RM^{\ell+1} Lx_{\text{fix}},$$

which is a system of two equations for the two-dimensional variable  $x_{\text{fix}}$  and the parameter  $u$  (results will be shown for healing time  $\ell = 1$ ). One of the fixed points is of saddle type. We compute the stable manifold of the saddle fixed point using the algorithm for maps that are not globally invertible, proposed by England *et al* [10] and originally implemented for two-dimensional maps in `DsTool`. Since the map  $\mathcal{M}_\ell$  is implicitly defined, the algorithm as originally implemented would require the solution of the nonlinear system (9) every time the map gets evaluated. This turns out not to be necessary: with a small modification the stable manifold algorithm does not require any solution of a nonlinear system (see Appendix A for a brief explanation). The stable manifold of the saddle fixed point will determine the basin of attraction for the stable fixed point (the other fixed point is a source for all  $u$ ) on the slow manifold.

The large amplitude response (attracting initial conditions on the other side of the stable manifold) is partially outside of the domain of validity of the coordinates introduced by lifting  $L$  and restriction  $R$ . Figure 6b shows the curve in the domain  $L$  plane along which the Jacobian of  $RM^1L$  becomes singular, which violates one of the assumptions made in the implicit definition (9) of  $\mathcal{M}_1$ . Outside of this curve (where the large amplitude solution lies), our chosen plane

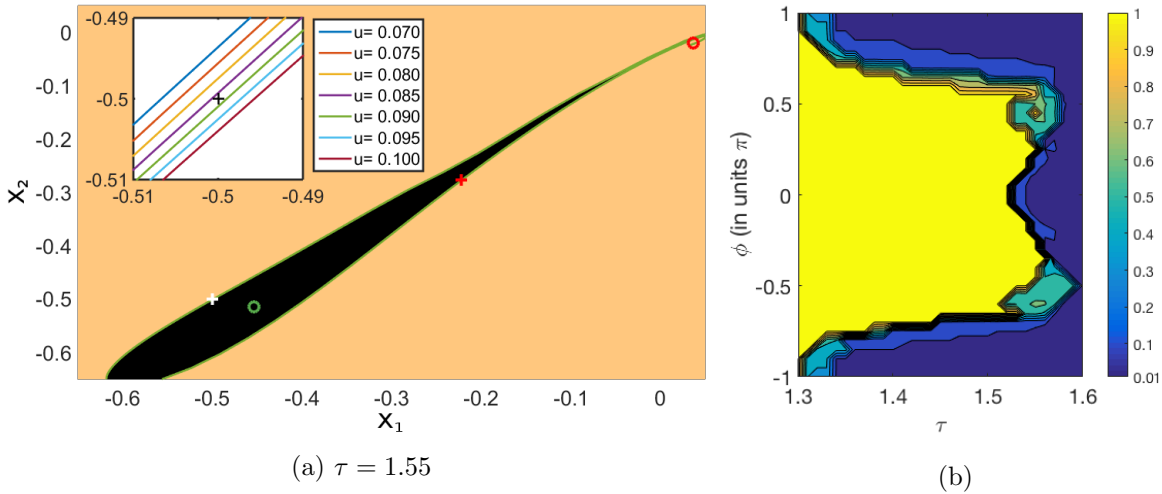


Figure 7: (a) Basin of attraction for the small amplitude stable periodic orbit for  $\tau = 1.55$ . Initial conditions in the black regions are attracted to the small amplitude stable periodic orbit (green circle) intersected with  $\text{dom } L$ . The white cross indicates the initial condition  $(x_1, x_2) = (-0.5, -0.5)$  used to create Figure 4b. The red circle is the unstable small amplitude periodic orbit, while the red cross represents the saddle periodic orbit. Figure zoom in top left shows stable manifold for different values of  $u$  close to the initial condition  $(x_1, x_2) = (-0.5, -0.5)$  (black cross). (b) Threshold values for  $u$  at which a transition to the large-amplitude response is observed as a function of delay  $\tau$  and phase shift  $\phi$ . Values for which no transitions were observed are shown with  $u = 1$ . Other parameters for both figures:  $T = 4.1$ ,  $p = 0.95$ ,  $r = s = 0.8$ ; initial condition  $X_0 = -0.5$ .

is no longer valid. However, the spectral gap values indicate that the dynamics may still be confined to a two-dimensional slow manifold.

**3.3. Basins of attraction and stable manifold in the plane.** Figure 7a shows the basins in the rectangle  $[-0.65, 0.05] \times [-0.65, 0.05]$  for  $u = 0.09$ .

The constant history  $Lx$  with  $x_1 = x_2 = -0.5$ , corresponding to an initial head point  $y_0$  and initial history  $\tilde{y}$  both equal to  $-0.5$ , was used in the parameter scan for increasing forcing amplitude  $u$ , depicted in Figure 4b. This point is indicated by a white cross in Figure 7a. Black regions in Figure 7a are initial values in  $\text{dom } L$  that converge to the stable small-amplitude periodic orbit in the center of the black region. The beige region contains initial conditions that escape to the large amplitude response. The saddle fixed point is located near  $(-0.2, -0.3)$ . Its stable manifold (in green) is the boundary between the two basins of attraction. The inset in Figure 7a shows how the stable manifold of the saddle fixed point changes as the forcing amplitude  $u$  increases. In particular, we observe how the initial condition  $(-0.5, -0.5)^T$  is crossed by the stable manifold, which shifts downward as  $u$  increases. An animation of the moving basin of attraction with increasing  $u$  can be found in the supplementary material.

**3.4. Dependence on forcing phase.** As the basin of attraction in Figure 7a shows, the critical forcing amplitude  $u = 0.09$  for the transition depends strongly on the initial condition, which we chose as  $X_0 = -0.5$  for the heat map in Figure 4b. A simple alternative way to illustrate the importance of the initial condition is to vary the phase of the periodic forcing. We adjust the forcing equation accordingly,

$$(10) \quad F_P(t) = \sin((2\pi/T)t - \phi), \quad \phi \in [-\pi, \pi].$$

The variable  $\phi$  represents the phase shift of the forcing. Note that the bifurcation diagram Figure 5a is independent of the forcing phase  $\phi$ . However, Figure 7b shows that the phase affects the threshold value for the forcing amplitude  $u$  at which a transition to the large-amplitude response occurs for initial value  $X_0 = -0.5$ . Figure 7b shows contours of the smallest value of  $u$  for which we observe a transition to large-amplitude response in simulations for different forcing phases  $\phi$  and delays  $\tau$  in the bistable region  $r_{\text{el}}$  of Figure 2. For all points in 7b we chose the initial value  $X_0 = -0.5$ . For some parameter combinations the response is always small amplitude. In these points we set the contour level to its maximum ( $u = 1$ ). A distinct boundary can be seen between parameter combinations that exhibit transitions at low values of  $u$  and those that do not. For a forcing phase  $\phi = \pi$ , a transition can always occur within the bistable region.

In the supplementary material we show the effect of a phase shift on the basin of attraction for the small-amplitude periodic orbit in the plane  $\text{dom } L$ . This implies that, for some phases  $\phi$ , trajectories from the initial history  $X_0 = -0.5$  will converge to the small amplitude periodic orbit, while for other phases trajectories starting from  $X_0 = -0.5$  will converge to the large amplitude response.

**4. Conclusions.** We have presented a study of a scalar DDE model for the Pleistocene when subjected to periodic forcing. The forcing period is 41 kyr, corresponding to the most prominent frequency seen in astronomical insolation variations. With this particular forcing, two stable solutions are observed at small forcing amplitudes: a small-amplitude periodic orbit and a large-amplitude, long-period response. Both responses are a perturbation to the stable solutions of the autonomous system. When the forcing amplitude is varied, we observe a threshold between convergence to the periodic orbit and convergence to the large-amplitude response. Numerical bifurcation analysis of the small-amplitude periodic orbit shows that this threshold is outside of the region where any bifurcations occur. In addition, the bifurcation analysis illustrates that no bifurcation occurs for  $\tau < 1.53$ . This implies that even a change in the forcing amplitude (e.g. a modulated envelope of the periodic forcing) is not enough to cause the temporal transition observed with the quasiperiodic forcing. This supports the conclusions of [29] that the phenomenon observed in Figure 3a is not related to a slow passage through a classical bifurcation, including bifurcations of periodic orbits. This is different from the idea presented in [9], where in simple oscillator models under periodic forcing a generic transcritical bifurcation is necessary for the system to transition between the smaller-amplitude 40kyr cycle to the large amplitude 100kyr response. We therefore conjecture it is an effect of the quasiperiodicity of the astronomical forcing in combination with the coexisting autonomous attractors. This may require application of the general quasiperiodic theory of Fuhrmann *et al.* [12] or the pullback attractor framework outlined in Chekroun *et al.* [5].

In order to consider basins of attraction, we show that there exists a two-dimensional slow manifold on which a stable saddle, and unstable periodic orbit persist. We employ equation-free methods to construct a stroboscopic map on the slow manifold and track the locations of its fixed points. In addition, we compute the stable manifold of the saddle fixed point, which forms the boundary for the basin of attraction of the stable periodic orbit. From this we observe the the basin boundary moves with the increasing forcing amplitude. It crosses our chosen initial condition for an amplitude around  $u = 0.09$ . The basin of attraction is also shown to be affected by the phase of the forcing. We conclude that the threshold behavior observed for the periodically forced model can be attributed to a shifting basin of attraction.

Thus, for periodic forcing our observation of a transition to large-amplitude response depends strongly on the choice of initial condition. This is not the case for the quasiperiodic forcing extracted from astronomic data in Figure 1. Quinn *et al.* [29] showed that finite-time Lyapunov exponents (FTLEs) along the trajectories in Figure 3a remain negative for  $u < 0.22$  prior to transition time ( $\sim 750$  kyr BP). This implies that the transition in time and in  $u$  (at  $u = 0.08$ ) seen in Figure 3a is locally independent of initial conditions. Therefore the threshold behavior seen in Figure 3a when increasing  $u$  cannot be attributed solely to a moving basin of attraction. Although a bifurcation was not the cause for the periodically forced system, we cannot rule out the existence of a nonautonomous bifurcation associated with the quasiperiodically forced system. An initial study of the nonautonomous dynamics with astronomical forcing from Figure 1 suggests that the non-autonomous saddle of (2) (emerging from the saddle equilibrium at forcing amplitude  $u = 0$ ) and the non-autonomous pullback attractor (emerging from the stable equilibrium at  $u = 0$ ) undergo a non-smooth saddle-node bifurcation [12].

**Appendix A. Summary of modification of stable manifold algorithm by England, Osinga and Krauskopf [10].** The supplementary material describes how one can modify the search circle (SC) algorithm for stable manifolds in [10] for maps  $\mathcal{M}_\ell$  given implicitly through

$$(11) \quad \mathcal{M}_\ell : \text{dom } L \ni x \mapsto y \in \text{dom } L, \quad \text{where } y \text{ is the solution of } RM^{\ell+1}Lx = RM^\ell Ly.$$

The supplement also contains a didactic implementation in Matlab (Gnu Octave compatible) of the algorithm, a demonstration script reproducing the manifold in Figure 7a, and scripts reproducing some benchmark test examples from [10] (for the shear map, the modified Ikeda map and the primary stable curve of the modified Gumowski map; see [10] for a review of the properties and history of these examples).

The original SC algorithm [10] grows the stable curve of a map  $\mathcal{M}_\ell$  iteratively, approximating the stable curve by a (linear) interpolation of a sequence of  $k$  points  $S^k = (x^0, \dots, x^k)$  in  $\mathbb{R}^2$ . At step  $k+1$  a point  $x^{k+1}$  is added. The new point  $x^{k+1}$  lies on a search circle arc with a small adaptively chosen radius  $\Delta$  around  $x^k$ . The point  $x^{k+1}$  is defined by the requirement that it is an intersection of the image of this search circle under  $\mathcal{M}_\ell$  with the previously computed curve  $S^k$ . In particular, the algorithm [10] does not rely on root-finding using Newton iterations, but rather on a bisection to find the intersection between image of the search circle and previous manifold. In principle, this algorithm could be applied directly, if one solves the defining system (11),  $RM^{\ell+1}Lx = RM^\ell Ly$ , for  $y$  every time the original algorithm applies its map (in our case  $\mathcal{M}_\ell$ ) to a point  $x \in \mathbb{R}^2$ . However, a modification of the SC algorithm avoids

the need to solve the nonlinear equation (11). Instead of a single sequence (and interpolating curve)  $S^k$  one maintains two curves,  $S_L^k = (x_L^0, \dots, x_L^k)$  in  $\text{dom } L$  and  $S_R^k = (x_R^0, \dots, x_R^k)$  in  $\text{rg } R$ , with  $x_R^j = RM^\ell L x_L^j$ . Then one searches for  $x_L^{k+1}$  by finding an intersection of the map  $RM^{\ell+1}L$  image of the search circle of radius  $\Delta$  around  $x_L^k$  in  $\text{dom } L$  with the curve  $S_R^k$  in  $\text{rg } R$  (note the power  $\ell + 1$  in the mapping). Once one found this point  $x_L^{k+1}$ , for which  $RM^{\ell+1}L x_L^{k+1} \in S_R^k$ , one adds  $x_L^{k+1}$  to  $S_L^k$  and  $x_R^{k+1} = RM^\ell L x_L^{k+1}$  (note the power  $\ell$  of  $M$  in the mapping) to  $S_R^k$ . Otherwise, the same rules on angles and radii for acceptance of points apply as in [10].

**Acknowledgments.** We would like to thank the following people for their valuable discussions and input: Timothy Lenton, Peter Ashwin, Peter Ditlevsen, Martin Rasmussen, Tobias Jäger, Flavia Remo, Hassan Alkhayuon, Paul Ritchie, and Damian Smug.

## REFERENCES

- [1] P. ASHWIN, C. D. CAMP, AND A. S. VON DER HEYDT, *Chaotic and non-chaotic response to quasiperiodic forcing: limits to predictability of ice ages paced by milankovitch forcing*, Dynamics and Statistics of the Climate System, (2018).
- [2] A. L. BERGER, *Long-term variations of daily insolation and quaternary climatic changes*, Journal of the atmospheric sciences, 35 (1978), pp. 2362–2367.
- [3] K. BHATTACHARYA, M. GHIL, AND I. VULIS, *Internal variability of an energy-balance model with delayed albedo effects*, Journal of the Atmospheric Sciences, 39 (1982), pp. 1747–1773.
- [4] M. I. BUDYKO, *The effect of solar radiation variations on the climate of the earth*, tellus, 21 (1969), pp. 611–619.
- [5] M. D. CHEKROUN, M. GHIL, AND J. D. NEELIN, *Pullback attractor crisis in a delay differential enso model*, in Advances in Nonlinear Geosciences, Springer, 2018, pp. 1–33.
- [6] M. CRUCIFIX, *Oscillators and relaxation phenomena in pleistocene climate theory*, Phil. Trans. R. Soc. A, 370 (2012), pp. 1140–1165.
- [7] O. DIEKMANN, S. VAN GILS, S. VERDUYN LUNEL, AND H.-O. WALTHER, *Delay equations*, vol. 110 of Applied Mathematical Sciences, Springer-Verlag, New York, 1995.
- [8] H. A. DIJKSTRA, *Nonlinear climate dynamics*, Cambridge University Press, 2013.
- [9] P. D. DITLEVSEN AND P. ASHWIN, *Complex climate response to astronomical forcing: The middle-pleistocene transition in glacial cycles and changes in frequency locking*, (2018).
- [10] J. P. ENGLAND, B. KRAUSKOPF, AND H. M. OSINGA, *Computing one-dimensional stable manifolds and stable sets of planar maps without the inverse*, SIAM Journal on Applied Dynamical Systems, 3 (2004), pp. 161–190.
- [11] H. ENGLER, H. G. KAPER, T. J. KAPER, AND T. VO, *Modeling the dynamics of glacial cycles*, arXiv preprint arXiv:1705.07387, (2017).
- [12] G. FUHRMANN, M. GRÖGER, AND T. JÄGER, *Non-smooth saddle-node bifurcations II: dimensions of strange attractors*, Ergodic Theory and Dynamical Systems, (2017), pp. 1–23.
- [13] M. GHIL, A. MULLHAUPT, AND P. PESTIAUX, *Deep water formation and quaternary glaciations*, Climate dynamics, 2 (1987), pp. 1–10.
- [14] J. D. HAYS, J. IMBRIE, AND N. J. SHACKLETON, *Variations in the earth's orbit: pacemaker of the ice ages*, Science, 194 (1976), pp. 1121–1132.
- [15] P. HUYBERS, *Early pleistocene glacial cycles and the integrated summer insolation forcing*, Science, 313 (2006), pp. 508–511.
- [16] P. HUYBERS AND I. EISENMAN, *Integrated summer insolation calculations. noaa/ncdc paleoclimatology program data contribution# 2006-079*, 2006.
- [17] J. IMBRIE AND K. P. IMBRIE, *Ice ages: solving the mystery*, Harvard University Press, 1986.
- [18] H. KAPER AND H. ENGLER, *Mathematics and Climate*, Society for Industrial and Applied Mathematics, 2013.

- [19] Y. KEVREKIDIS AND G. SAMAÉY, *Equation-free multiscale computation: algorithms and applications*, Review of Physical Chemistry, 60 (2009), pp. 321–344.
- [20] Y. KEVREKIDIS AND G. SAMAÉY, *Equation-free modeling*, Scholarpedia, 5 (2010), p. 4847.
- [21] L. E. LISIECKI AND M. E. RAYMO, *A pliocene-pleistocene stack of 57 globally distributed benthic  $\delta^{18}\text{O}$  records*, Paleoceanography, 20 (2005).
- [22] K. MAASCH, *Statistical detection of the mid-pleistocene transition*, Climate dynamics, 2 (1988), pp. 133–143.
- [23] K. A. MAASCH AND B. SALTZMAN, *A low-order dynamical model of global climatic variability over the full pleistocene*, Journal of Geophysical Research: Atmospheres, 95 (1990), pp. 1955–1963.
- [24] J. MALLET-PARET AND G. R. SELL, *The poincaré–bendixson theorem for monotone cyclic feedback systems with delay*, Journal of differential equations, 125 (1996), pp. 441–489.
- [25] J. MALLET-PARET AND H. L. SMITH, *The poincaré–bendixson theorem for monotone cyclic feedback systems*, Journal of Dynamics and Differential Equations, 2 (1990), pp. 367–421.
- [26] M. MILANKOVITCH, *History of radiation on the earth and its use for the problem of the ice ages*, K. Serb. Akad. Beogr, (1941).
- [27] D. PAILLARD, *Quaternary glaciations: from observations to theories*, Quaternary Science Reviews, 107 (2015), pp. 11–24.
- [28] D. PAILLARD AND F. PARRENIN, *The antarctic ice sheet and the triggering of deglaciations*, Earth and Planetary Science Letters, 227 (2004), pp. 263–271.
- [29] C. QUINN, J. SIEBER, A. S. VON DER HEYDT, AND T. M. LENTON, *The mid-pleistocene transition induced by delayed feedback and bistability*, (2017).
- [30] B. SALTZMAN AND K. A. MAASCH, *Carbon cycle instability as a cause of the late pleistocene ice age oscillations: modeling the asymmetric response*, Global biogeochemical cycles, 2 (1988), pp. 177–185.
- [31] B. SALTZMAN AND K. A. MAASCH, *A first-order global model of late cenozoic climatic change ii. further analysis based on a simplification of co<sub>2</sub> dynamics*, Climate Dynamics, 5 (1991), pp. 201–210.
- [32] W. D. SELLERS, *A global climatic model based on the energy balance of the earth-atmosphere system*, Journal of Applied Meteorology, 8 (1969), pp. 392–400.
- [33] J. SIEBER, C. MARSCHLER, AND J. STARKE, *Convergence of equation-free methods in the case of finite time scale separation with application to stochastic systems*, arXiv preprint arXiv:1701.08999, (2017).